# Nonlinear modelling and adaptive control of smart rotor wind turbines

Juan Li [1,2], Yinan Wang [1], Shuyue Lin[3], Xiaowei Zhao[1,*]

[1] *Intelligent Control & Smart Energy (ICSE) Research Group, School of Engineering, University of Warwick, Coventry CV4 7AL, United Kingdom*
[2] *Department of Engineering, King's College London, London WC2R 2ND, United Kingdom*
[3] *Department of engineering, University of Hull, Hull HU6 7RX, United Kingdom*

**Abstract**

This paper develops a nonlinear mid-fidelity aeroservoelastic model for smart rotor wind turbines and studies the turbulent load alleviation of the wind turbines with trailing edge flaps (TEFs) actuated by a novel proportional-derivative model-free adaptive control (PD-MFAC) algorithm. This nonlinear model contains a structural model for the tower and blades represented by geometrically non-linear composite beams and an aerodynamic model for the rotor using a vortex panel method coupled with a stall delay process. The capability of the new aerodynamic model to deal with flow separations and analyze the detailed flow field enables it to simulate the dynamic response of the wind turbine blade sections with TEFs with arbitrary size and deflection angles. It is shown that the TEF alters the aerodynamic coefficients in a complex manner which could be explained by the evolution of the detailed vortical field. Furthermore, three independent PD-MFAC TEF controllers are designed to alleviate the turbulent load acting on the wind turbines. The effectiveness of the controller in terms of turbulent load alleviation is evaluated by the root mean square value of the blade root-bending moment (RBM). A traditional Gain-scheduled PI (GS-PI) controller is also designed as a comparison to the PD-MFAC controller. Simulation results show that to reduce the RBM and blade tip deflection (BTD) caused by external disturbances, the PD-MFAC flap controller shows more effective performance than the GS-PI flap controllers.

*Keywords:* Aeroelastic load alleviation, model-free adaptive control (MFAC), nonlinear system, wind turbine, smart rotor

*corresponding author
*Email address:* Xiaowei.Zhao@warwick.ac.uk (Xiaowei Zhao )

## 1. Introduction

To reduce greenhouse gas (GHG) emissions and achieve energy sustainability, renewable energies are becoming one of the most popular energy sources in the world. Among different renewable energy types, wind power is standing out as one of the fastest-growing and competitively commercialized energy sources [1]. It is expected to increase its global demand by up to 60% by the year 2050. To increase the average power capacity and decrease the Levelized Cost of Energy (LCOE), continuous efforts have been made in the design of larger wind turbines with an increasing rotor diameter, and hub height [2]. To this end, it is inevitable to have a more flexible and slender design for longer and heavier blades. As is well established, due to the inflow turbulence, wind shear, tower shadow, wake effects, gravity, mass and aerodynamic imbalances, and other sources of disturbance, wind turbines are subject to significant fluctuating loads in different frequency domains. Some of these unsteady loads may cause blade structural resonance and fatigue damage, some of those may contribute to structural failure and lead to a reduction of life expectancy [3]. The increasing size of wind turbine blades is accompanied by an increase in the susceptibility to gravitational effects and in wind speed variations across the rotor disk, which add difficulties in mitigating the fluctuating loads acting on the flexible blades. New challenges have been brought about in both modeling and control design of wind turbines. The development of higher fidelity models and the optimization of various flow-control devices to reduce the fluctuating loads, prolong the service life of the wind turbines, will be of great significance for the following years [4].

In terms of numerical models of horizontal axis wind turbines (HAWTs), a structural model and an aerodynamic model are combined to build a full aeroservoelastic model. There are mainly two categories of structural models according to the discretization methods used to present the flexible bodies, i.e. three-dimensional (3D) finite-element method (FEM) and one-dimensional (1D) composite beam models. 3D FEM is an extraordinary method to obtain detailed stress distributions within a structure. However, it is too computationally expensive to be used in testing the control strategies. There are linear composite beam models and nonlinear composite beam models. The most commonly used linear beam formulations are the classical Euler–Bernoulli beam theories and the Timoshenko beam theories for straight and uniform beams, containing the assumption of small displacements [5]. The latter contains shear deformation effects, while the former does not. The wind turbine blades normally have a thin and slender structure where the shear deformations effects are negligible, thus the Euler–Bernoulli beam theory is more often used for simplicity. Furthermore,

linear beam models are no longer sufficient to determine the large deformations and highly nonlinear structural response on a smart rotor wind turbine structure. Thus geometrically-exact composite beam theory, developed from the original Euler-Bernoulli beam theory by enabling non-uniform deforming of the cross-section within the linear regime, was developed [6]. There are a wide variety of approaches to modeling HAWT aerodynamics, ranging from the commonly used blade element momentum (BEM) method [7], the actuator type models [8], the free vortex wake (FVW) models [9, 10], and the unsteady vortex lattice methods (UVLM) [11, 12, 13] to higher fidelity methods, such as the CFD methods [14]. CFD models are the most accurate while the most computationally intensive models among others. BEM is the least computational cost while with the lowest accuracy. To provide a good balance between the computational cost and the accuracy, this work will propose a nonlinear aeroservoelastic model which includes a nonlinear Euler–Bernoulli beam theory and a discrete vortex method.

In terms of the control strategies in the load alleviation of wind turbines, there are two main categories, i.e. passive and active load alleviation methods. Examples of passive load alleviation strategies include morphing structures on wind turbine blades [15]. Such passive load alleviation systems are normally not easily maintainable [16]. Among the active control methods, individual blade pitch control (IPC) which alters the aerodynamic properties of the blades is the most widely studied in the past [16, 17, 18]. Rezaeiha et al. [19] studied the total fatigue loads on the wind turbines caused by different sources and showed that wind turbulence results in over 65% of flapwise fatigue, while gravity contributes to over 80% of edgewise fatigue. The low-frequency deterministic loads, caused by wind shear, tower shadow or gravity, could be well reduced by IPC, while for mitigating the high-frequency non-deterministic loads, e.g. turbulent load, on wind turbine blades, IPC is less effective due to its reaction speed restricted by the actuator limitations. Moreover, using IPC to mitigate the blades' fatigue load is compensated by an increase in pitch activity, thus the design of IPC is a trade-off between the fatigue damage of the blades and blade pitch actuators [20]. Thus, the concept of 'smart rotor control' has been proposed for a more precise and responsive turbulence load alleviation of wind turbine blades as a compliment to IPC [21, 22]. The main advantage of the smart rotor is dealing with high-frequency loads caused by turbulence rather than the low-frequency deterministic load. Smart rotors refer to the distributed control surfaces equipped on turbine blades that can be actuated rapidly. Among different types of 'smart rotors', the trailing-edge flaps (TEFs) demonstrated excellence in mitigating loads on wind turbines.

Table.1 exhibits the examples of state-of-the-art techniques on the load alleviation of wind turbines

| Model | TEF configuration | Control Algorithm | reduction in blade RBM | Reference |
|---|---|---|---|---|
| Aeroelastic code HAWC2 (BEM-based) | 10% chord, $\pm 10^o$ | Linear quadratic (LQ) control algorithm | 14% | Bergami & Poulsen, 2015 [23] |
| An aero-hydro-servoelastic model (UVLM-based) | 10% chord, $\pm 10^o$ | $H_\infty$ | 4.68-13.2% | Ng et al., 2017 [13] |
| NREL's FAST/AeroDyn + CFD with $k-\omega$ shear stress transport (SST) model | 20% chord, $\pm 5^o$ | Gain scheduling PI controller | 5.48-19.5% | Sun et al., 2017 [24] |
| A modified version of FAST combined with XFOIL and CFD | 25% chord, $\pm 10^o$ (Optimized) | PID / DMC | 8-42% | Zhang et al., 2018 [25] |
| BEM-based method coupled with CFD | 25% chord, $\pm 9^o$ | Feedback linearization-based | 33.0-42.5% | Zhang et al., 2018 [26] |
| BEM-based | 10% chord, $\pm 15^o$ | CPFC with an azimuth angle feed-forward and a loads feedback control strategy | 53.7% | He et al., 2018 [27] |
| UIUC Appied Aerodynamics Group's PROPID (BEM-based) | 4% chord, $\pm 10^o$ | Feedback loop controller | 15% | Samara & Johnson, 2020 [22] |
| NREL's OpenFAST + XFoil (A linear characteristic assumption) | 20% chord, $\pm 10^o$ | Generic PI | $> 6$ % | Feil et al., 2020 [28] |

Table 1: A tabular comparison of state-of-the-art smart rotor techniques on the load alleviation of wind turbine rotors. TEF = trailing edge flap; RBM = root bending moment; UVLM = unsteady vortex lattice method; UIUC = The University of Illinois Urbana-Champaign; BEM = blade element momentum; NREL = National Renewable Energy Laboratory; PI = proportional-integral; PID = proportional-integral-derivative; DMC = dynamic matrix control; CFD = computational fluid dynamics; CPFC = Combined individual pitch control and TEF flap control.

using TEFs. Note that the (flap-wise or in-plane) blade root bending moment (RBM), one of the typical full-blade performance parameters, is a widely used parameter in the literature to study the fatigue and extreme load in the wind turbine industry. Moreover, in the field test, it is easy to measure the root bending moment. Thus, the reduction in the oscillation of RBM is demonstrated here to show the control efficiency. Several research gaps still exist in these previous studies.

i. In the numerical simulation and control design of wind turbines with controllable flaps, the UVLM-based and the BEM-based aerodynamic models are commonly used. The BEM method requires a series of empirical corrections and may overestimate some aerodynamic loads, while

a traditional UVLM model makes an attached flow assumption. Neither of these models deals with the separating flows which could regularly be discovered in wind turbine flows. Higher-order aerodynamic models such as non-linear lifting line free vortex wake (LLFVW) models could include the non-linearity in wind turbine modeling, where the strength of the lifting line is not got by satisfying the normal velocity boundary condition at selected points on the blade but instead from an experimental $C_L - \alpha$ curve for the lift of the airfoil section. Similarly, for a smart rotor configuration, the strength of the lifting line is determined by the non-linear coefficient data of the flap deflection. However, the non-linear LLFVW model can not simulate the detailed flow field evolution. Moreover, a large amount of empirical coefficient data are required from either CFD or experiments. Those data change with different wind turbine blade geometry, different flap sizes, and different flap angles.

ii. The involvement of CFD could largely improve the accuracy of the model when dealing with complex flows such as separating flows. However, high-precision CFD computations consume a large amount of computing resources and are limited to specific shapes.

iii. Most of the model-based smart rotor control schemes in the literature (e.g. $H_\infty$ control [13]) for HAWTs show a satisfactory load alleviation effect. Nevertheless, for highly nonlinear models, there is a limited load reduction performance of model-based controllers. Traditional model-free control strategies, e.g. proportional-integral-derivative (PID) controller and Gain scheduling proportional-integral (PI) controller, only gave a limited reduction of the load. The parameters in a PID control scheme depend on the specific operating conditions, therefore the control efficiency will be inevitably reduced in off-design conditions.

In our previous paper [29], a novel proportional-derivative model-free adaptive control (PD-MFAC) scheme has been developed and tested on a preliminary low-fidelity model of a wind turbine configuration. In the PD-MFAC, in order to build a linearized equivalent dynamical model along the dynamic operation points of the original nonlinear single-input single-output (SISO) system, a pseudo partial derivative (PPD) is introduced. The PPD is determined by the real-time measurements of the input and output data of the controlled closed-loop system. The PD-MFAC offers both improved performance and applicability. In the proposed PD-MFAC flap control scheme, the features of the dynamic wind turbine system with smart rotors, e.g. the coupling of the time-dependent nonlinear aerodynamic and structural characteristics, are estimated by the PPD vector. The introduction of the PPD vector transfer the original model into an equivalent online data

model. Thereby, contrary to the traditional model-based control schemes, the unstable responses and the possible degradation of the performance due to the order-reduction could be avoided. The developed PD-MFAC has the robustness dealing with dynamic systems with high complexity at different operating conditions. It is shown that the PD-MFAC system achieves higher load reduction than both the classical model-based control algorithms, such as $H_\infty$ controller, and the well-studied model-free method, such as the Gain-scheduled proportional-integral (GS-PI) controller.

This work focus on the alleviation of the flapwise fluctuation loads caused by the inflow turbulence by actively adjusting the trailing-edge flap angle. To address the research gaps in the modeling and control of large wind turbines, the objectives of the present work are twofold: (1) to construct a nonlinear vortex panel with stall delay model for the aerodynamic simulation of the HAWT actuated with the smart rotor; (2) to design three independent model-free adaptive TEF controllers to achieve desirable dynamic turbulent load alleviation of the HAWT. Simulation studies are carried out to evaluate the efficiency of our designed PD-MFAC in the reduction of the root-bending moment (RBM) and blade tip deflection (BTD) on a highly nonlinear smart rotor wind turbine model. GS-PI controllers are also designed and tested on this new model as a comparison to the proposed PD-MFAC. Quantitative studies on the probability density distribution along with the power spectral density in the frequency domain are also performed to further prove the superiority of the proposed PD-MFAC strategy.

In Section 2, the aeroservoelastic wind turbine model including a newly developed unsteady aerodynamic model considering the trailing edge flap deflection is described. In Section 3, the MFAC flap controller is designed for load alleviation, and a GS-PI controller is also designed as comparison. In Section 4, numerical results of the open-loop simulation, the MFAC control and the GS-PI control are given. In Section 5, concluding remarks are given.

## 2. Numerical method

The aeroservoelastic model of a wind turbine [30] with smart rotors will be adapted from the low-fidelity model developed in our previous work [29]. Although the proposed aeroelastic model is eligible for modern large and flexible wind turbines, we still use the NREL 5MW model wind turbine as an example to demonstrate and validate our new model. The new model consists of a structural model and an aerodynamic model. The structural model is directly inherited from the previous work, while a nonlinear aerodynamic model is newly developed here based on the vortex

panel method (VPM). This new aerodynamic model is a mid-fidelity replacement of the linear strip theory and the thin airfoil theory in the previous work. It is capable of incorporating the nonlinear effect caused by the flow separation and dynamic stall. This section will first recall the structural model based on the nonlinear composite beam model, finally demonstrate the development of the aerodynamic model based on VPM. In this work, the same wind turbine (NREL 5-MW reference wind turbine) configuration as in Li et al.(2021)[29] is continuously used for the aeroservoelastic modeling and control design. The basic parameters for the wind turbine configuration and the static aerodynamic properties for the blade sections of the reference wind turbine ($C_{L\alpha}$, $C_{L0}$, $C_{D0}$ and $C_{M0}$) could be found in our previous paper[29].

In the numerical simulations, the wind turbine is operating in a turbulent wind field with a mean inflow speed $V_\infty$ and a specific turbulent intensity. The turbulence inflow data $w_\delta$, in accordance with the International Electrotechnical Commission (IEC) standard 61400-1 [31], will be generated by a well-known open-source stochastic inflow turbulence tool (TurbSim) developed by National Renewable Energy Laboratory (NREL). As the considered model wind turbine has a rated wind speed of 11.4 m/s, mean wind speeds of 11m/s and 14m/s are chosen to cover the typical operating speed range. As the turbulence intensity at the mean wind speed of 11 -14 m/s ranges from 5% to 20%[32], three typical turbulent intensities from this range are chosen, they are $6\%, 10\%$ and 17.5%, respectively. The von Karman turbulence model and the Normal Turbulence Model (NTM) with different turbulence seeds are chosen in TurbSim. Yaw angles are not considered since it is out of the scope of this work.

### *2.1. Structural Model*

The same structural model as in the previous work[29] is adopted here. It is a full 6-degree of freedom (DOF) geometrically-nonlinear Euler-Bernoulli beam model where the tower and the blades are defined as a collection of geometrically nonlinear composite beams respectively. The wind turbine configuration and its discrete multi-body composite beam representation are shown in Fig. 1. The intrinsic beam formulations are closed as follows according to Hamilton's principle,

$$\begin{pmatrix} \mathbf{M}_s & \mathbf{0} \\ \mathbf{0} & \mathbf{C}_s \end{pmatrix} \dot{\mathbf{x}} = \begin{pmatrix} -\mathcal{L}_1(\mathbf{x}_1)\mathbf{M}_s & \frac{\partial}{\partial s} + \mathbf{E} - \mathcal{L}_2(\mathbf{x}_2)\mathbf{C}_s \\ \frac{\partial}{\partial s} - \mathbf{E}^\top & \mathcal{L}_1^\top(\mathbf{x}_1)\mathbf{C}_s \end{pmatrix} \mathbf{x} - \begin{pmatrix} \mathbf{f}_A \\ \mathbf{0} \end{pmatrix}, \tag{1}$$

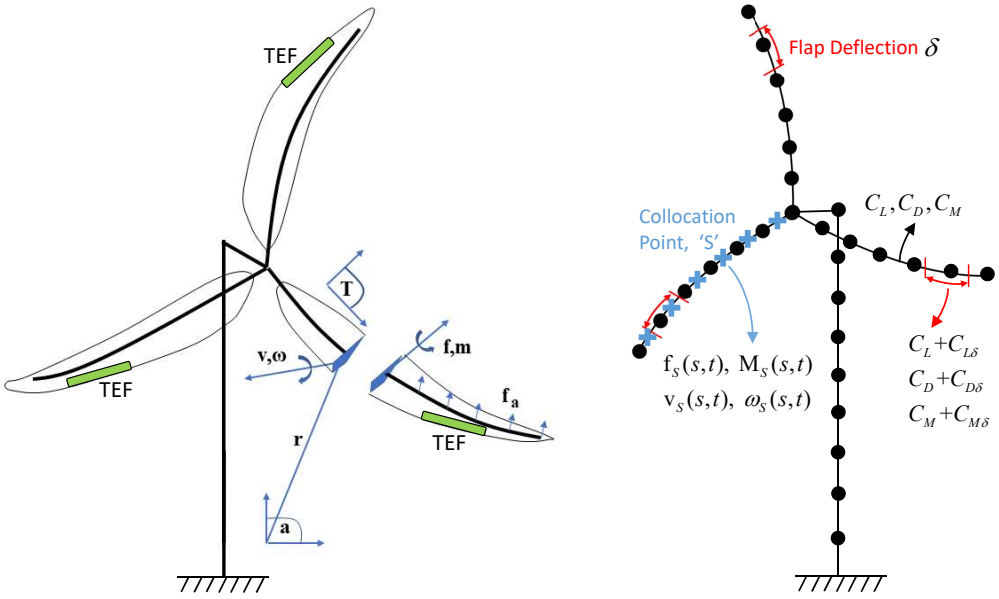


Figure 1: The multi-body configuration (left) and the discrete multi-body aerodynamic and structural model (right) of the HAWT. The associated structural dynamic quantities are marked, where the symbol **a** indicates the inertial frame ('**a**-frame'), and the symbol **T** indicates the local frame ('**T**-frame'). TEF = trailing edge flap.

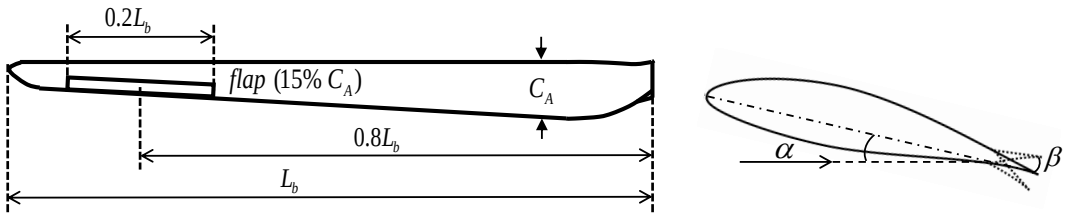


Figure 2: Smart rotor blade configuration. Left: the wind turbine blade with a trailing edge flap (TEF), which occupies 20% span, 15% local chord and is located at a mean position of 80% span; Right: the airfoil at a typical cross-section of the wing is at a local incidence of $\alpha$, and the flap angle is $\beta$ (positive when deflects downward).

where $\mathbf{x} = [\ \mathbf{x}_1^\top \quad \mathbf{x}_2^\top\ ]^\top$ is the state variables at $s$, the operator $\mathcal{L}_1$ is introduced to convert a 6-element state vector into a matrix, and $\mathbf{E} = \mathcal{L}_1([\ 1 \quad 0 \quad 0 \quad 0 \quad 0 \quad 0\ ]^\top)$ is a constant matrix. $\mathbf{M}_s(s)$ and $\mathbf{C}_s(s)$ are the beam-equivalent sectional mass and compliance matrices at a local coordinate of $s$. The total external force is denoted as $\mathbf{f}_A$. For the details of the structural model please refer to Li et al. (2021)[29]. In this work, a bigger flap size is considered for better control performance than the small flaps. The TEF configuration considered here takes up 20% of the wingspan and 15% of the local chord as shown in Fig. 2. We will model the dynamics of the TEF by modifying the shape of the wing sections (the airfoils) continuously, instead of modifying the local aerodynamic coefficients of the lifting surface. In Fig. 2, the local angle of attack is denoted as $\alpha$, while the flap deflection angle is denoted as $\beta$.

### *2.2. Aerodynamic model*

The aerodynamic model is a vortex panel method with a stall delay algorithm, where the separation position is intuitively taken as the main parameter to be determined. The vortex panel method for a blade section with a TEF is shown in Fig.3. A total number of $N-1$ panels ($VS_i, i = 1, 2, ..., N-1$) are allocated on the body surface. Each of the panels is represented by a linear distribution of vorticity. The effects of the control surfaces (the trailing edge flaps) are incorporated by modifying the shape of the body at each time step. The steady-state separation point is prescribed and provided by XFoil or experimental data in lookup tables. A dynamic stall delay algorithm is introduced to determine the dynamic separation point.

In subsection 2.2.1, we will recall the standard VPM, and in subsection 2.2.2, we will introduce the dynamic stall delay model to determine the dynamic separation point. Since the state-space description of the aerodynamic model is the same as in our previous paper[29], we omitted the detailed formulas here.

#### *2.2.1. Vortex panel model (VPM)*

Given the specific geometry of the airfoil deformation and the dynamic separation position, the problem described in Fig. 3 becomes a standard VPM. In this model, the $N+3$ unknown parameters, $\gamma_i$ (i = 1,2,...,N), $\gamma_{TE}$, $\gamma_{SEP}$, and $\sigma$, are solved by Neumann non-penetration condition at the center of each $VS_i$ ($\nabla\mathbf{\Phi}_i \cdot \boldsymbol{n}_i = 0, i = 1, 2, ..., N-1$), the Kutta condition at the trailing edge ($\gamma_1 + \gamma_N = \gamma_{TE}$), the vorticity continuity at the separation point and trailing edge ($\gamma_{SEP} = \gamma_{i=i_{SEP}}, \gamma_N = 0$),

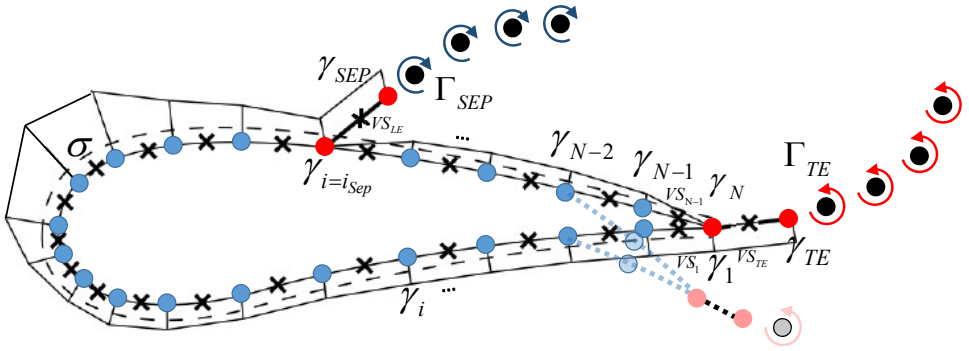


Figure 3: Schematic display of the singularity distributions in the panel method for separated flows. The vorticity strength at each end of the panel is denoted as $\gamma_i$ (i = 1,2,..., N). A trailing edge vortex sheet $VS_{TE}$ with a strength of $\gamma_{TE}$ is released at the trailing edge, and another vortex sheet $VS_{LE}$ with a strength of $\gamma_{SEP}$ is released at separating point $i = i_{Sep}$ to account for the flow separation. A constant source $\sigma$ distribution is applied over the airfoil.

and the implementation of Kelvin's theorem ($(\gamma_{SEP}\Delta l_{SEP})^t + (\gamma_{TE}\Delta l_{TE})^t = \Gamma_B^t - \Gamma_B^{t-1}$). Here $t$ and $t-1$ refer to the current time step and the last time step respectively, and $\Delta l_{SEP}, \Delta l_{TE}$ are the length of the separating vortex sheet and the wake sheet respectively. Note that once the vorticity is shed to the flow field as point vortices, their strength remains constant in time until they are merged by coalescence. A coalescence criterion in the far wake has been used to restrict the total number of point vortices. In each time step, the strength of the vortex distributions are resolved, the induced velocity field and the velocity potential are then obtained. The reader could refer to Katz (1981)[33] for more details about solving the standard VPM. The local aerodynamic coefficients of the lifting surface $C_L$, $C_D$, and $C_M$ are obtained by integrating the pressure distribution over the airfoil given by the unsteady Bernoulli Equation

$$C_{p,i} = 1 - \frac{\boldsymbol{v}_i^2}{V_\infty^2} - \frac{2}{V_\infty^2}\frac{\partial \boldsymbol{\Phi}_i}{\partial t}. \tag{2}$$

This VPM has been validated with classical cases such as the starting flow around a thin airfoil at an incidence of $45^o$.

### 2.2.2. A dynamic stall model to determine the dynamic separation point

The steady-state separation point for a 2D airfoil with TEFs as a function of the AoA ($\alpha$) and the TEF deflection angle ($\beta$) could be obtained in several ways, such as XFOIL tool, the extended Kirchhoff's Law, or experimental measurements. For simplicity, here we will use an extended Kirchhoff's Law to determine the separation point of the airfoil with TEF. Here the steady-state lift coefficient is given by

$$C_L(\alpha,\beta) = C_L(\alpha)\big|_{\beta=0} + g(\alpha)\left.\frac{\partial C_L}{\partial \beta}\right|_{\alpha=0}\beta, \tag{3}$$

where $g(\alpha)$ is a empirical parameter which satisfies $g(0^o) = 1, g(90^o) = 0$. According to the experimental results [34], the steady lift coefficient is proportional to the flap deflection in a certain range of small angles of attack. Thus here we choose $g(\alpha) = f^{st}(\alpha)$ as an approximation. Subsequently, the steady airfoil trailing edge separation point $f^{st}(\alpha,\beta)$ could then be obtained from the extended Kirchoff's flow equation.

$$f^{st}(\alpha,\beta) = (2\sqrt{\frac{C_L(\alpha,\beta)}{C_{L,\alpha}(\beta=0)(\alpha-\alpha_0)}} - 1)^2. \tag{4}$$

With the steady-state separation points given, two time lags, i.e. the time-lag due to the LE pressure ($T_p$) and the time-lag due to the dynamics of the boundary layer ($T_f$) are introduced here to calculate the dynamic (stall-delayed) separation points. The dynamic separation point after the first delay is determined by

$$\begin{aligned} \frac{dC_L^{p'}(t)}{dt} + \frac{1}{T_p}C_L^{p'}(t) &= \frac{1}{T_p}C_L^{p}(t), \\ \alpha_{eqv}(t) &= \frac{C_L^{p'}(t)}{C_{L,\alpha}} + \alpha_0, \\ f'(t) &= f^{st}\left(\alpha_{eqv}(t),\beta\right), \end{aligned} \tag{5}$$

where $C_L^p(t)$ is the unsteady lift coefficient for attached flow, and $T_p = 1.7$ is the time constant for the separated flow [35]. $C_L^{p'}(t)$ is the lift coefficient with a time-lag to the attached flow lift coefficient $C_L^p(t)$. Likewise, the dynamic separation point after the second time lag is determined

by

$$\frac{df''(t)}{dt} + \frac{1}{T_f} f''(t) = \frac{1}{T_f} f'(t). \tag{6}$$

where $T_f = 3$ is the time constant for the separated flow which can be determined from unsteady aerofoil data [35]. To validate the dynamic stall algorithm coupled with the VPM for predicting the aerodynamic coefficients, we compare the experimental aerodynamic coefficients of an airfoil (NACA 4415) which has similar dynamic responses as NACA64_A17 with the force coefficients obtained by our model in different dynamic cases [36]: (a) $\alpha = 8^o \pm 10^o sin(\omega t)$; (b) $\alpha = 14^o \pm 10^o sin(\omega t)$; (c) $\alpha = 20^o \pm 10^o sin(\omega t)$; (d) $\alpha = 8^o \pm 5^o sin(\omega t)$; (e) $\alpha = 14^o \pm 5^o sin(\omega t)$; (f) $\alpha = 20^o \pm 5^o sin(\omega t)$. The comparison results are shown in figures 4, 5, and 6 for the lift coefficient, the drag coefficient, and the moment coefficient, respectively. We can see from these figures that our model compares well with the experimental data.

Moreover, the comparison of the lift coefficient hysteresis curves with different flap dynamics $\beta = 10^o sin(\omega t + \phi)$ ($\phi = 0$, $\pi/2$, and $\pi$) are shown in Fig. 7. The smart rotor shows similar dynamic lift responses as the experimental results in Raiola et al. (2018) [34]. For different phase delays $\phi$ with respect to the pitching motion of the main airfoil, the lift coefficient loops $1 \to 2 \to 3 \to 4 \to 1$ have different shapes. The effect of TEF dynamics on the lift coefficient for the case of pitching angle $\alpha = 8^o \pm 10^o sin(\omega t)$ is depicted in Fig. 7 (a), and the influence of $\phi$ on the lift coefficient for the case of pitching angle $\alpha = 14^o \pm 10^o sin(\omega t)$ is shown in Fig. 7 (b). In both figures, it is shown that the lift coefficient loops rotate counterclockwise for $\phi = 0$, i.e., the TEF deflection angle is in phase with the airfoil pitching angle. On the contrary, both of the lift coefficient loops rotate clockwise $\phi = \pi$, i.e., the TEF deflection angle and the airfoil pitching angle are in phase opposition. Among all different phase differences, $\phi = \pi/2$ causes the maximized amplitude of the lift coefficient hysteresis cycle.

The above phenomena could be well explained by the detailed vortex field evolution shown in Fig. 8 for the case of $\alpha = 14^o \pm 10^o sin(\omega t)$. When the angle of attack approaches the mean value in the down-stroke (point '1' in Fig. 8 (b)), the reason for the lowest lift coefficient in the case of $\phi = \pi/2$ are three folds: 1 - the TEF deflection against the camber-line disturbs the big separating bubble above the airfoil, thus weakens the low-pressure area on the upper surface of the airfoil and reduces the lift coefficient; 2 - the TEF deflection reduces the equivalent curvature of the airfoil, thus reduces the linearized lift coefficient; 3 - the TEF deflection causes the rolling up of a trailing

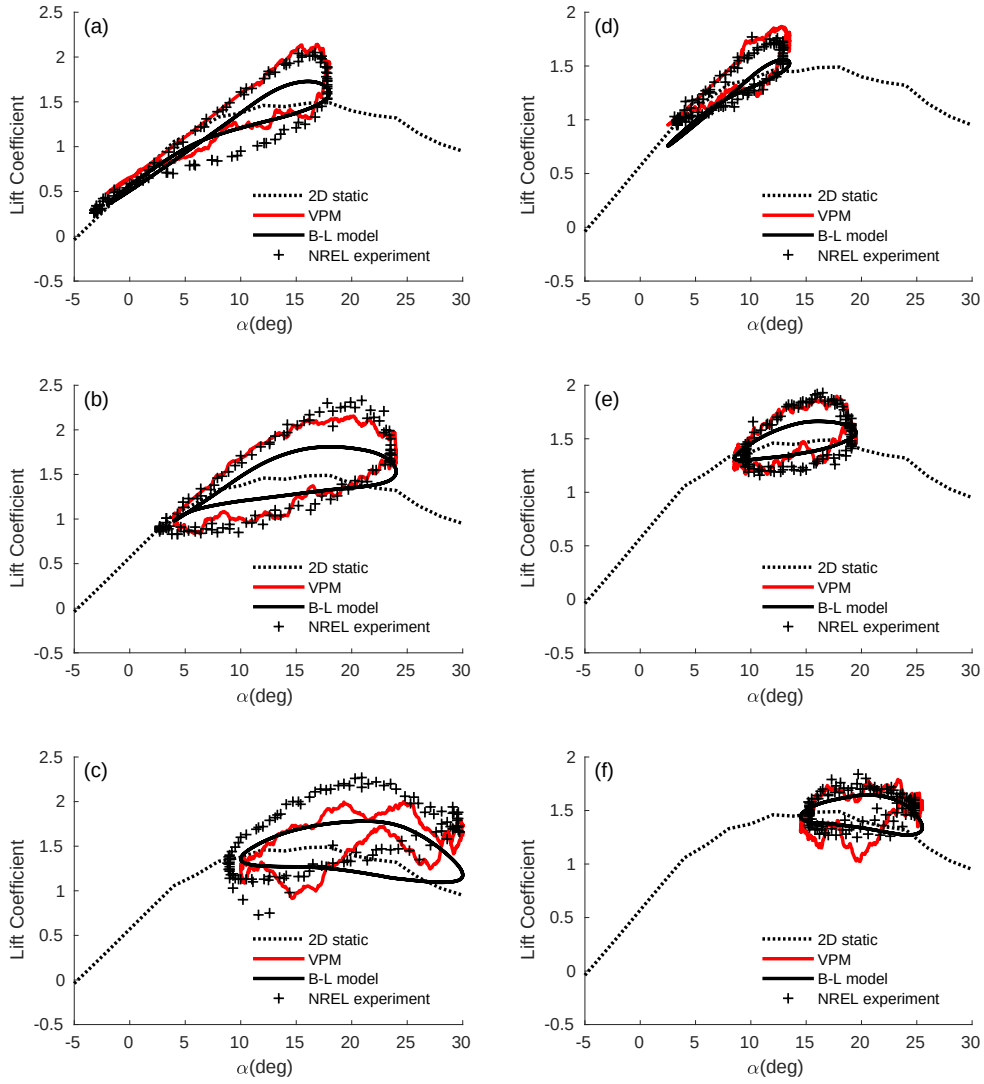


Figure 4: Comparison between dynamic stall models for a NACA64_A17 airfoil and the experimental lift coefficient results for a NACA4415 airfoil [36] at various mean angles of attack for a reduced frequency $k = \omega c/(2V_\infty) = 0.1$. (a) $\alpha = 8^o \pm 10^o sin(\omega t)$; (b) $\alpha = 14^o \pm 10^o sin(\omega t)$; (c) $\alpha = 20^o \pm 10^o sin(\omega t)$; (d) $\alpha = 8^o \pm 5^o sin(\omega t)$; (e) $\alpha = 14^o \pm 5^o sin(\omega t)$; (f) $\alpha = 20^o \pm 5^o sin(\omega t)$.

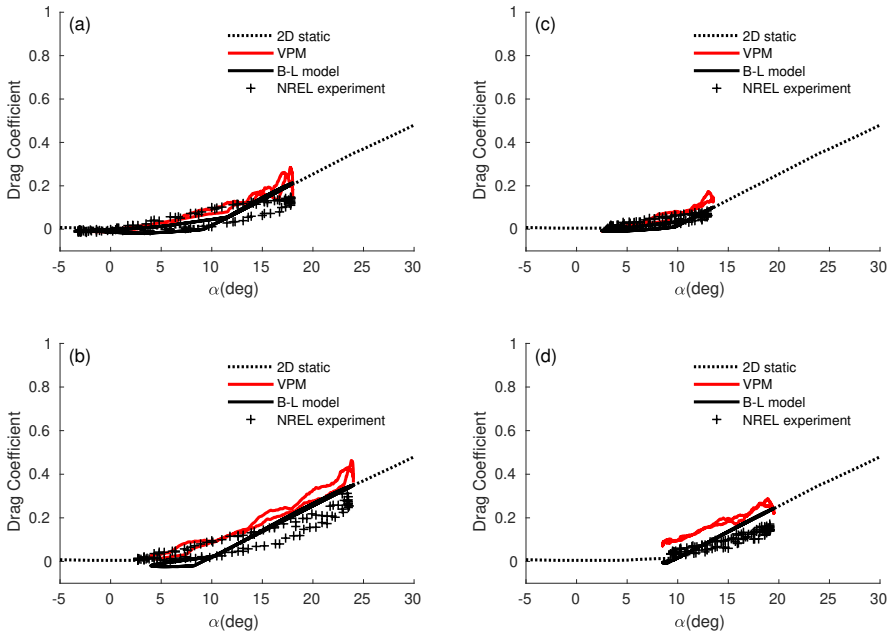


Figure 5: Comparison between dynamic stall models for a NACA64_A17 airfoil and the experimental drag coefficient results for a NACA4415 airfoil [36] at various mean angles of attack for a reduced frequency $k = \omega c/(2V_\infty) = 0.1$. (a) $\alpha = 8^o \pm 10^o sin(\omega t)$; (b) $\alpha = 14^o \pm 10^o sin(\omega t)$; (c) $\alpha = 8^o \pm 5^o sin(\omega t)$; (d) $\alpha = 14^o \pm 5^o sin(\omega t)$.

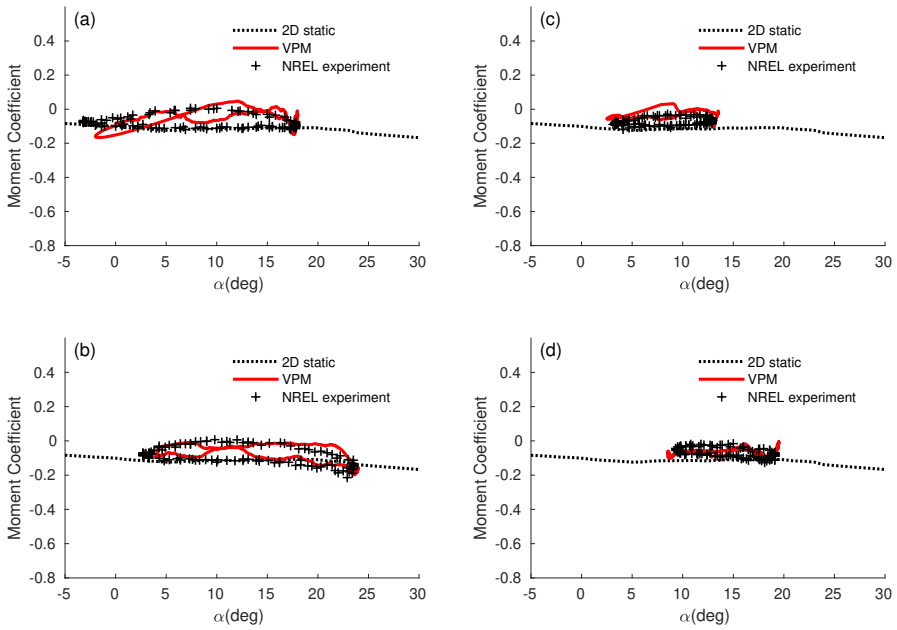


Figure 6: Comparison between dynamic stall models for a NACA64_A17 airfoil and the experimental moment coefficient results for a NACA4415 airfoil [36] at various mean angles of attack for a reduced frequency $k = \omega c/(2V_\infty) = 0.1$. (a) $\alpha = 8^o \pm 10^o sin(\omega t)$; (b) $\alpha = 14^o \pm 10^o sin(\omega t)$; (c) $\alpha = 8^o \pm 5^o sin(\omega t)$; (d) $\alpha = 14^o \pm 5^o sin(\omega t)$.

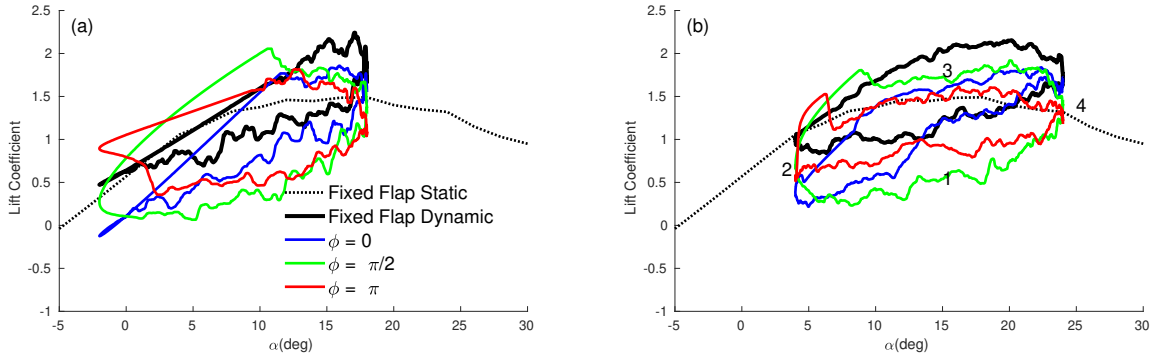


Figure 7: Comparison of dynamic stall behavior for the lift coefficient on a NACA64_A17 airfoil with different TEF dynamics $\beta = 10^o sin(\omega t + \phi)$ ($\phi = 0$, $\pi/2$, and $\pi$). (a) $\alpha = 8^o \pm 10^o sin(\omega t)$; (b) $\alpha = 14^o \pm 10^o sin(\omega t)$.

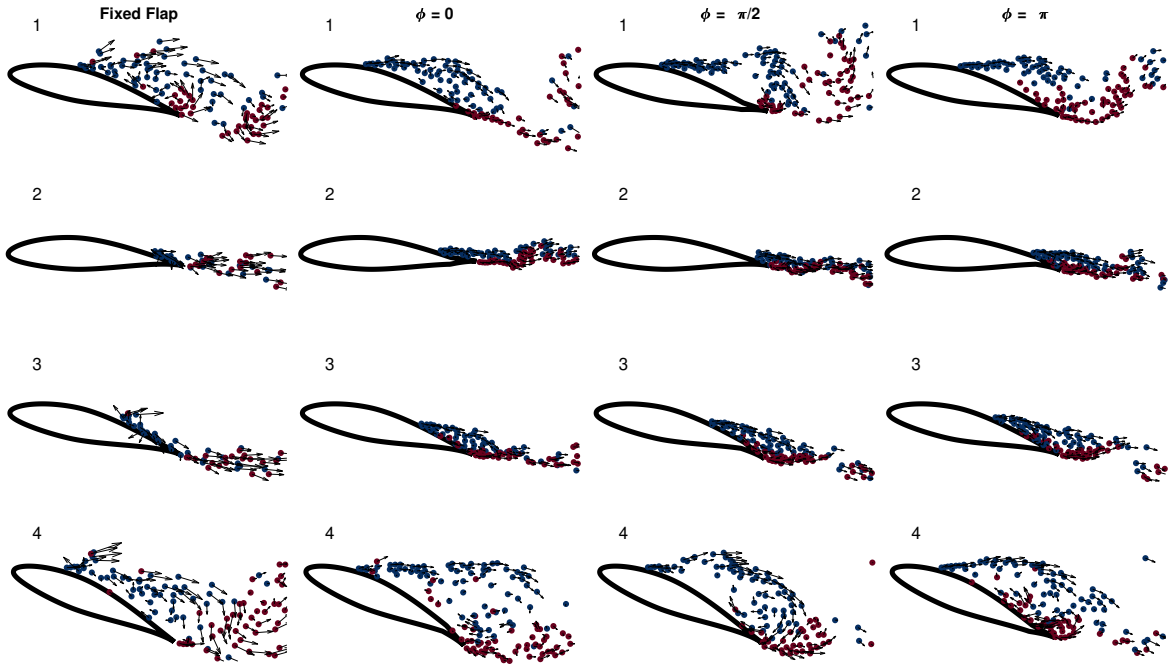


Figure 8: The detailed vortex field evolution at four typical instants during the dynamic stall for the cases of $\alpha = 14^o \pm 10^o sin(\omega t)$ without TEF, and with different TEF dynamics $\beta = 10^o sin(\omega t + \phi)$ ($\phi = 0$, $\pi/2$, and $\pi$). The red solid dots represent the counterclockwise rotating point vortex, while the blue solid dots represent the clockwise rotating point vortex. The black arrows on each solid point show the local velocity of each point vortex.

edge vortex, which reduces the lift coefficient through an upwash effect on the lower surface of the TE. When the angle attack is at the lowest value (point '2' in Fig. 8 (b)) or approaching the mean value in the up-stroke (point '3' in in Fig. 8 (b)), the lift coefficients mainly depend on the linear effects. At point '2', the in-phase flap deflection ($\phi = 0$) with respect to the angle of attack causes an equivalent negative curvature which causes a decrease in the lift coefficient. On the contrary, the opposite-phase flap deflection ($\phi = \pi$) causes an equivalent positive curvature, which increases the linear lift coefficient. At point '3', all the cases with flap deflection cause the rolling-up of a separating vortex at the trailing edge, which breaks the stall delay effect, thus decrease the lift coefficient compared with the case without TEF. At point '4' when the angle of attack reaches the peak value, the flow is completely separated and highly nonlinear. The lift coefficients are not affected by the TEF deflection anymore.

Similarly, the comparison of the drag coefficient hysteresis curves with different flap dynamics $\beta = 10^o sin(\omega t + \phi)$ ($\phi = 0$, $\pi/2$, and $\pi$) are shown in Fig. 9. The comparison results for the moment coefficients are shown in Fig. 10. The drag coefficients and the moment coefficients could be analyzed similarly to the lift coefficients. For the relative small angle of attack case ($\alpha = 8^o \pm 10^o sin(\omega t)$) in Fig. 9 (a) and Fig. 10 (a), we can see that the drag coefficient hysteresis curves rotates clockwise and the the moment coefficient hysteresis curves rotates counterclockwise when phase difference $\phi$ increases from 0 to $\pi$. It is not difficult to understand that the aerodynamic characteristics are governed by linear effects within most of this angle range. On the contrary, it becomes more complicated for a larger average angle of attack case, since the aerodynamics are now dominated by nonlinear effects as shown in Figures 9 (b) and 10 (b). When combined with 8, the effect of TEF deflection on the aerodynamic drag and moment on a dynamic stall airfoil could be well explained in a similar way as its effect on the lift.

## 3. Control system design

Three independent and identical flap angle controllers driven by either the PD-MFAC algorithm (9) or the traditional GS-PI scheme are designed for the mitigation of the RBM fluctuation on each blade. The objective of this control system is to minimize fluctuation of the root bending moment (RBM) caused by turbulence on each blade. The input data of the PD-MFAC controllers are the real-time measurement of the RBM on three blades, and the control output of the PD-MFAC

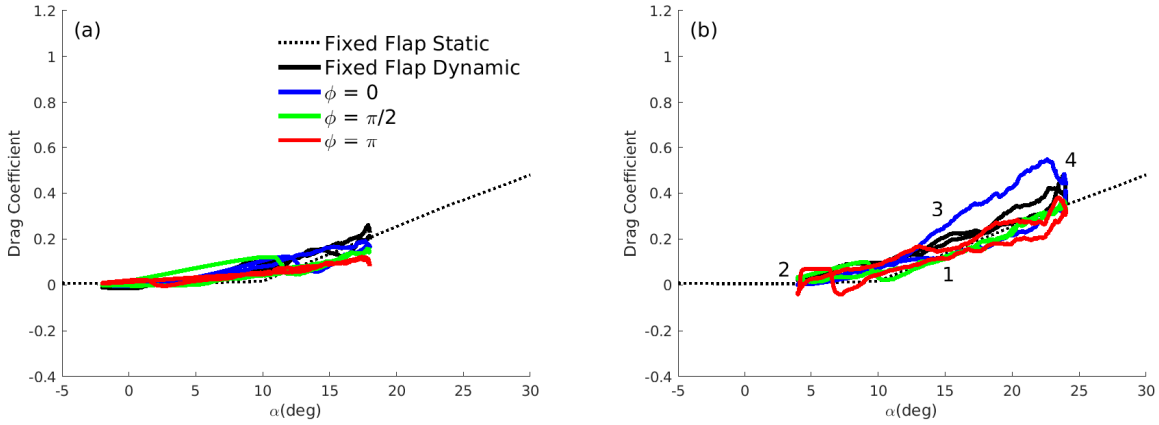


Figure 9: Comparison of dynamic stall behavior for the drag coefficients on a NACA64_A17 airfoil with different TEF dynamics $\beta = 10^o sin(\omega t + \phi)$ ($\phi = 0$, $\pi/2$, and $\pi$). (a) $\alpha = 8^o \pm 10^o sin(\omega t)$; (b) $\alpha = 14^o \pm 10^o sin(\omega t)$.

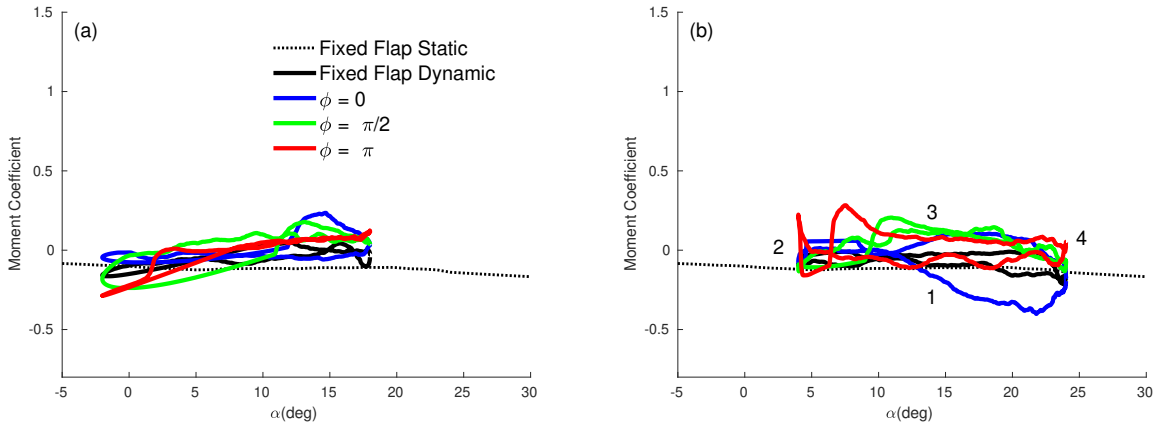


Figure 10: Comparison of dynamic stall behavior for the moment coefficients on a NACA64_A17 airfoil with different TEF dynamics $\beta = 10^o sin(\omega t + \phi)$ ($\phi = 0$, $\pi/2$, and $\pi$). (a) $\alpha = 8^o \pm 10^o sin(\omega t)$; (b) $\alpha = 14^o \pm 10^o sin(\omega t)$.

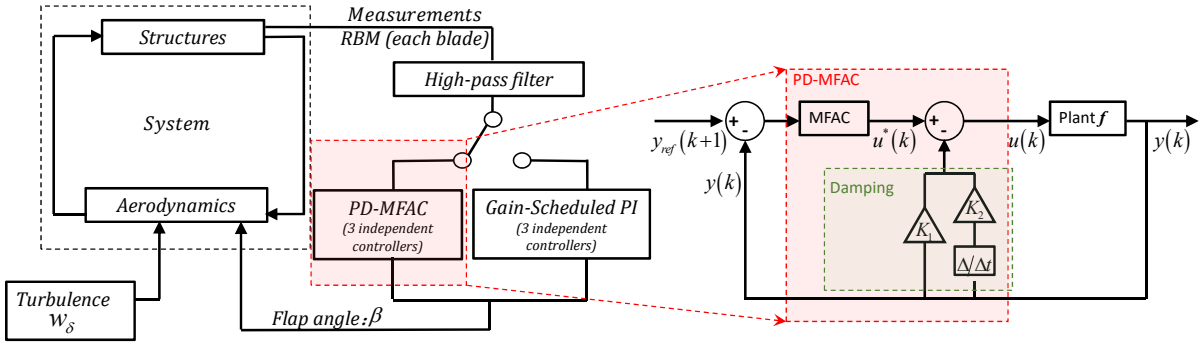


Figure 11: Closed-loop block diagram of the fluid-structure coupling and control system, with a detailed control structure of the PD-MFAC scheme.

controllers are three flap pitch angles. A closed-loop block diagram of the fluid-structure coupling and control system is depicted in Fig. 11.

The derivation and the stability analysis of the PD-MFAC algorithm could be found in our previous work [29]. Here we only give the final expression of this algorithm and the parameters. For a SISO nonlinear system expressed in the time discrete form

$$y\left(k+1\right)=f\left(y\left(k\right),...,y\left(k-n_y\right),u\left(k\right),...,u\left(k-n_u\right)\right), \tag{7}$$

where $u\left(k\right)$ is the input signal and $y\left(k\right)$ is the output of the nonlinear SISO system at discrete time $k$, $n_y$ and $n_u$ are the known orders, which are positive integers, a virtual control input (the input of the equivalent system shown in Fig. 11) is defined as

$$u^*\left(k\right)=u\left(k\right)+K_1y\left(k\right)+K_2\frac{\Delta y\left(k\right)}{\Delta t}, \tag{8}$$

where $K_1$ and $K_2$ are constant control parameters, $\Delta y\left(k\right)=y\left(k\right)-y\left(k-1\right)$ is the time difference of the system output, and $\Delta t$ is the time step for the discrete system. By introducing the PPD

vector $\boldsymbol{\phi}_L^*$, the system could be linearized along the operation point as follows

$$\Delta y\left(k+1\right)=\boldsymbol{\phi}_L^*\left(k\right)\Delta\boldsymbol{U}_L^*\left(k\right).$$

The PD-MFAC algorithm can be derived as

$$\begin{aligned}u(k)=u(k-1)+&\frac{\rho_1\hat{\phi}_1^*(k)(y_{ref}(k+1)-y(k))}{\lambda+\left|\hat{\phi}_1^*(k)\right|^2}-\frac{\hat{\phi}_1^*(k)\sum_{i=2}^{L}\rho_i\hat{\phi}_i^*(k)\Delta u^*(k-i+1)}{\lambda+\left|\hat{\phi}_1^*(k)\right|^2}\\&-sign\left(\widehat{\phi}_1^*\left(1\right)\right)\left(K_1\Delta y\left(k\right)+K_2\Delta\left(\frac{\Delta y\left(k\right)}{\Delta t}\right)\right),\end{aligned}\tag{9a}$$

$$\hat{\boldsymbol{\phi}}_L^*(k)=\hat{\boldsymbol{\phi}}_L^*(k-1)+\eta\Delta\boldsymbol{U}_L^*(k-1)*\frac{(\Delta y(k)-\hat{\boldsymbol{\phi}}_L^{*T}(k-1)\Delta\boldsymbol{U}_L^*(k-1))}{\mu+\left\|\Delta\boldsymbol{U}_L^*(k-1)\right\|^2}\tag{9b}$$

$$\hat{\boldsymbol{\phi}}_L^*(k)=\hat{\boldsymbol{\phi}}_L^*(1),\ if\ \left\|\hat{\boldsymbol{\phi}}_L^*(k)\right\|\leq\varepsilon,\ \text{or}\ \left\|\Delta U_L(^*k-1)\right\|\leq\varepsilon,\ \text{or}\ sign(\hat{\phi}_1^*(k))\neq sign(\hat{\phi}_1^*(1)).\tag{9c}$$

Here $\widehat{\boldsymbol{\phi}}_L^*\left(k\right)$ is an estimation of the PPD vector $\boldsymbol{\phi}_L^*\left(k\right)$. $\Delta\boldsymbol{U}_L^*\left(k\right)=\boldsymbol{U}_L^*\left(k\right)-\boldsymbol{U}_L^*\left(k-1\right)$ is the time difference of historical virtual control input vector $\boldsymbol{U}_L^*\left(k\right)$. The virtual control input vector is obtained by $\boldsymbol{U}_L^*\left(k\right)=\left[u^*\left(k\right),...,u^*\left(k-L+1\right)\right]$. For our considered case, $L=3$. The step factors $\rho_i\in(0,1]$ and $\eta\in(0,2]$, and the penalty factors satisfy $\lambda>0,\mu>0$.

The parameters in the PD-MFAC are tuned by using a particle swarm optimization (PSO) algorithm. In the PSO algorithm, the number of swarms is set to be 20 and the number of maximum iterations is set to be 50. The searching process will continue until the residual converges to 1e-12. Here is the results tuned for this PD-MFAC scheme: $k_1=9.8366\times10^{-08},K_2=3.91\times10^{-09},\lambda=8\times10^8,\rho=6.684\times10^{-3},\eta=9\times10^{-4},\mu=9\times10^{-3},\boldsymbol{\phi}_L^*\left(0\right)=[8.2\times10^6,8.2\times10^6,8.2\times10^6]^T$. Differing from our previous work, a wider saturation of $[-45^o,+45^o]$ is applied here to allow larger flap deflection angles when tuning our control parameters. However, as will be shown in the next section, in the close-loop simulations with our tuned control parameters, the flap deflects between $-15^o$ and $+15^o$. The reference control input is the RBM obtained by the open-loop simulation without any turbulence.

As a comparison to the proposed PD-MFAC scheme, a traditional GS-PI controller is also

designed. In this controller, the proportional and integral terms are defined as

$$K_P(y) = \frac{k_p}{1 + (y - y_{ref})/k_g},\ K_I(y) = -\frac{k_i}{1 + (y - y_{ref})/k_g}, \tag{10}$$

where $y$ is the flapwise RBM and $y_{ref}$ is the reference flapwise RBM when there is no inflow turbulence. The three parameters $k_p$, $k_i$, and $k_g$ in the GS-PI controller are also tuned by a PSO algorithm. The parameters obtained by the PSO algorithm are $k_p = 5.36e-02$, $k_i = 8.79e-08$, and $k_g = 9.8e08$.

## 4. Numerical Simulations

The open-loop and closed-loop numerical simulation of the NREL 5-MW reference wind turbine with TEFs will be carried out in this section. Using the aeroservoelastic modeling method described in Section 2, and the control strategies described in Section 3, the dynamic responses of the wind turbine configuration are simulated in a Matlab environment. We test the performance of both PD-MFAC TEF controllers and GS-PI TEF controllers. Three independent TEF controllers are mounted on three blades separately to alleviate the oscillations of the flapwise blade root bending moment (RBM) on each blade. The real-time variation of RBM on each blade is measured at every time step and sent to the PD-MFAC and GS-PI control system as the control input. Since the goal of this work is to alleviate the relative high-frequency load variation caused by turbulence, a high-pass filter is implemented before RBM signals are sent to the control system. The high-pass filter is designed to filter the low-frequency 1P, 2P, and 3P load of the model wind turbine and keep the load caused by the turbulent inflow wind. The low frequency oscillating loads could be easily dealt with by classical IPC, which is out of the scope of this work. A time step of 0.005 *second* is chosen for the numerical simulations. Convergence tests are carried out with three different time-steps 0.001, 0.003, and 0.005 *second*. For each free-stream velocity and turbulent intensity case, the wind turbine rotor is rotating at a speed of 12.1 *rpm*, and the simulation lasts 6450 time steps, i.e. 32.25 *seconds*, or 6.5 *cycles*. We are more concerned about high disturbance. Thus, the control parameters for both the PD-MFAC and the GS-PI controller are tuned in the case with the high disturbance (with an income velocity of $14m/s$ and turbulence intensity of 17.5%) among all six cases considered in this work. The time duration is chosen as a trade-off between the computational cost and the inclusion of as much as the load oscillation effects caused by the high-frequency turbulent

inflow. The open-loop and closed loop simulation results are shown in Fig.12 and Fig.13. Figure 12 demonstrates the results of several key indexes for the unsteady dynamics of the wind turbine systems with or without TEF controllers: (a) is the flapwise root bending moment (RBM); (b) is the root torsion moment (RTM); (c) is the flap deflection angle; and (d) is the blade tip deflections (BTD). The open-loop simulation results are indicated as solid black lines, the simulation results with PD-MFAC controllers are indicated as solid red lines, and the time-varying results with the GS-PI controllers are shown as solid green lines. From the Fig.12 (a)(d), we can see that both control strategies have largely alleviated the oscillating of RBM and BTD. Both controllers cannot suppress the oscillation of RTM as shown in Fig.12 (b). Due to the additional moment contributed by the TEF configuration, an inevitable increase in the fluctuation of blade RTM is observed for both controllers. In Fig.12 (c), we can see that the flap deflection angle varies in the range from $-15^o$ to $+15^o$. Figures 13 (a) and (b) show the probability density plots of the RBM and the BTD

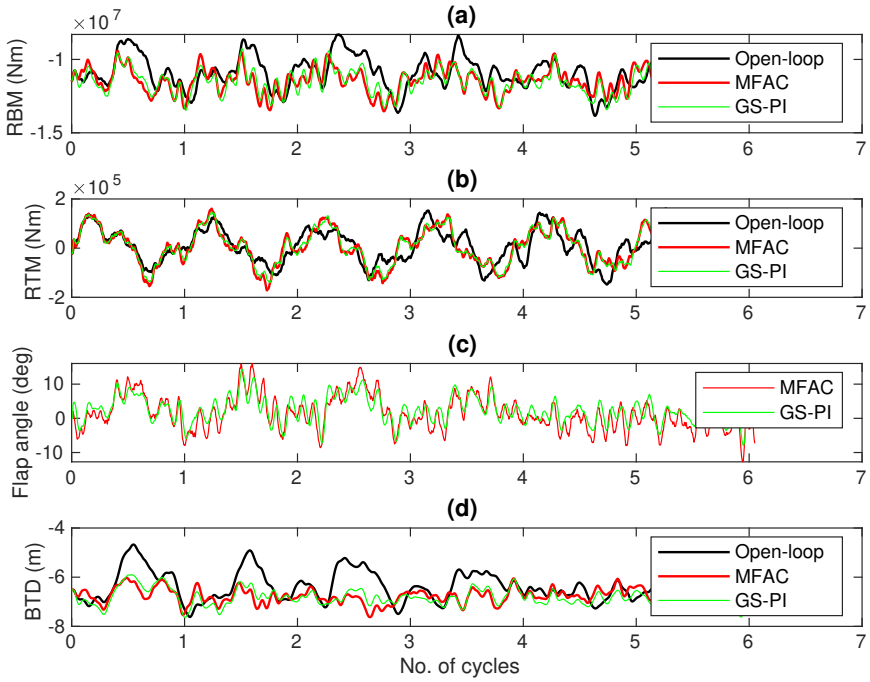


Figure 12: Open-loop and closed-loop time simulation results of (a) root bending moment; (b) root torsion moment; (c) flap angle and (d) blade tip deflection, at a flow velocity of $14m/s$ and turbulence intensity of 17.5%.

purely casued by turbulence, respectively. We can see from these figures that the density bars for the open-loop simulations are more centralized than those for the GS-PI controller simulations. And the density bars for the GS-PI controller simulations are more centralized than those for PD-MFAC simulations. Thus we can come to a conclusion that, an obvious reduction in the blade root load and the deformation deviations could be achieved through the TEF controllers. Moreover, the proposed PD-MFAC has better performance than the classical GS-PI. For the same case, the time sequence data of the flapwise RBM and the BTD purely caused by the turbulence are transformed into the frequency domain through discrete Fourier transformation. As a result, the comparison of the power spectral density (PSD) of RBM and BTD for different controllers and the open-loop simulation are shown in figures 13 (c) and (d). It is observed that both control strategies reduce the vibration in most of the frequency domain. With regard to the RBM, the PD-MFAC is slightly superior to the GS-PI in most of the frequency domains except for a middle frequency between 0.1 Hz and 0.2 Hz. For reducing the BTD oscillation, the PD-MFAC works just as well as the GS-PI at a low-frequency domain (<0.1 Hz), while the GS-PI reduces the displacement to a larger extent than the PD-MFAC at a higher frequency range.

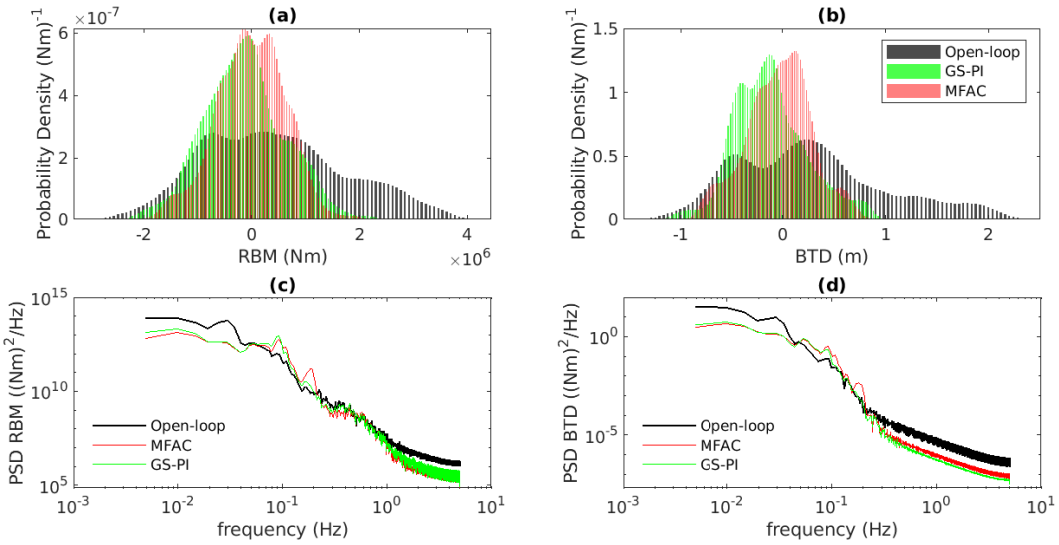


Figure 13: Probability density plot of (a) root bending moment (RBM); (b) blade tip deflection (BTD), and the power spectral density (PSD) of (c) root bending moment (RBM); (d) blade tip deflection (BTD), at a flow velocity of $14m/s$ and turbulence intensity of 17.5%.

For the case of a same turbulence intensity of 17.5% and a different flow velocity of $11m/s$, the simulation results are displayed in figures 14 and 15. Similar conclusions could be drawn from the previously designed case. The lower the mean wind velocity is, the smaller the flap deflection angle is needed to suppress the load caused by turbulence. For this specific case, the flap deflection angle varies between $-12^o$ and $+12^o$. Likewise, the TEF deflection causes a high-frequency small-amplitude oscillation of RTM, and the amplitude of oscillation caused by MFAC is larger than that of GS-PI. According to the probability density distribution plot (Fig. 15(a)(b)) and the PSD RBM plot (Fig. 15 (c)(d)), the PD-MFAC have a marked advantage over the GS-PI for the reduction of both RBM and BTD in most of the frequency domains.

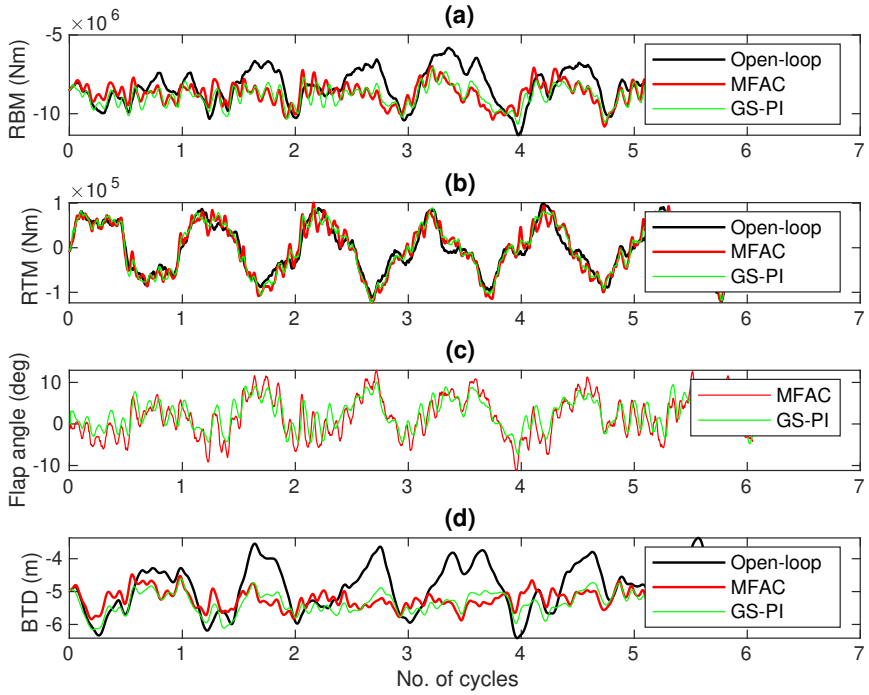


Figure 14: Open-loop and closed-loop time simulation results of (a) root bending moment; (b) root torsion moment; (c) flap angle and (d) blade tip deflection, at a flow velocity of $11m/s$ and turbulence intensity of 17.5%.

For an other case at a mean flow velocity of $11m/s$ and a turbulence intensity of 6%, the results for the time variation of the RBM, the RTM, the TEF deflection angle, and the BTD are shown in figures 16(a),(b),(c), and (d), respectively. In this specific case, the TEF deflection angle varies

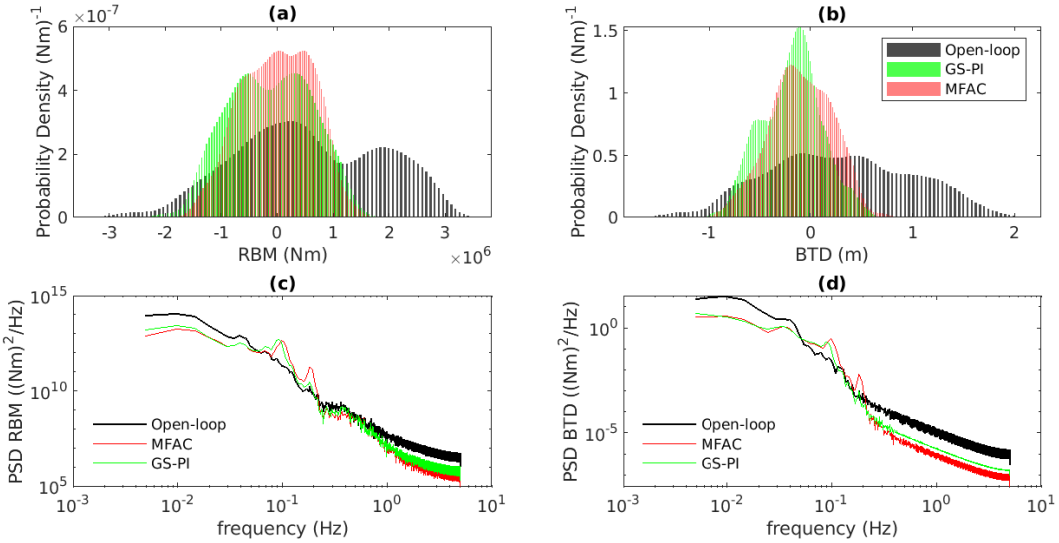


Figure 15: Probability density plot of (a) root bending moment (RBM); (b) blade tip deflection (BTD), and the power spectral density (PSD) of (c) root bending moment (RBM); (d) blade tip deflection (BTD), at a flow velocity of $11m/s$ and turbulence intensity of 17.5%.

between $-10^o$ and $+6^o$ as a control output to alleviate the unsteady load. The total reduction of the oscillating RBM, in this case, is not as significant as it was in the previous cases. This is because the control design of this work is targeted for the turbulent load, and a lower turbulent intensity here causes lower load oscillations. The probability density of RBM and BTD are shown in figures 17(a),(b), respectively. It is shown that the probability distribution of both RBM and BTD using PD-MFAC are centralized around 0, while those data obtained by using GS-PI are centralized around a negative value. Therefore, the performance of PD-MFAC in this case is substantially better than that of GS-PI. The PSD RBM and BTD in the frequency domain shown in figures 17(c) and (d) indicate that the PD-MFAC surpasses the GS-PI in most of the frequency domains except in a frequency between 0.1 Hz and 0.2 Hz.

Table 2 demonstrates the closed-loop alleviation of blade loads under 6 cases of different flow velocity and turbulence intensity with flaps actuated by the PD-MFAC controller and the GS-PI controller. An rms RBM reduction of 50.29 - 56.44% and an rms BTD reduction of 54.53 - 62.12% have been achieved using the PD-MFAC. Note that in this work, we consider the reductions of the high-frequency load mostly caused by the turbulence, while some other works consider the

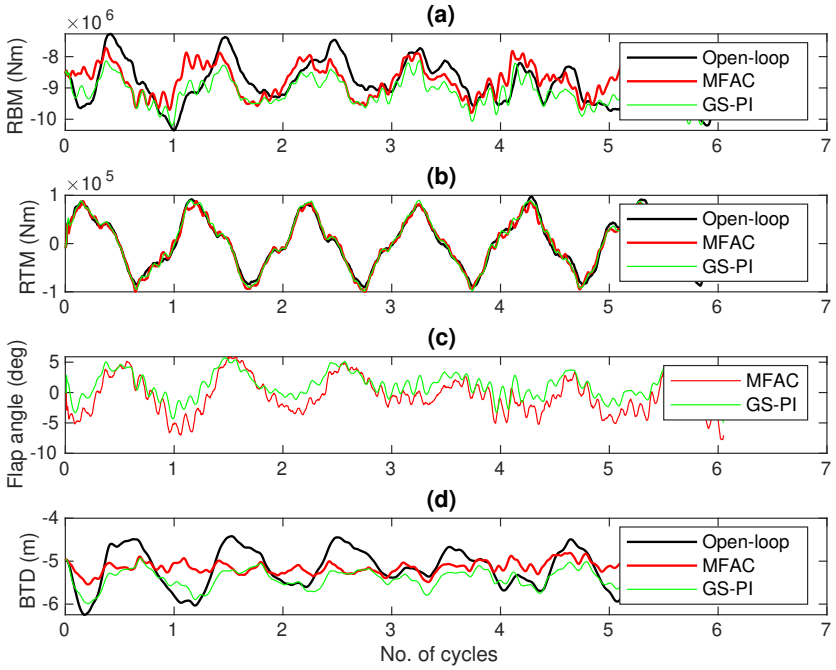


Figure 16: Open-loop and closed-loop time simulation results of (a) root bending moment; (b) root torsion moment; (c) flap angle and (d) blade tip deflection, at a flow velocity of $11m/s$ and turbulence intensity of 6%.

| **Cases** | **Flow (m/s)** | **TI (%)** | **MFAC % rd rms RBM** | **GS-PI % rd rms RBM** | **MFAC % rd rms BTD** | **GS-PI % rd rms BTD** |
|---|---|---|---|---|---|---|
| 1 | 14 | 17.5 | 53.82 | 44.54 | 58.30 | 51.32 |
| 2 | 14 | 10.0 | 50.29 | 37.46 | 55.34 | 37.28 |
| 3 | 14 | 6.0 | 55.27 | 34.96 | 62.12 | 36.37 |
| 4 | 11 | 17.5 | 55.08 | 46.99 | 57.41 | 54.08 |
| 5 | 11 | 10.0 | 54.01 | 25.77 | 54.53 | 36.22 |
| 6 | 11 | 6.0 | 56.44 | 26.45 | 58.62 | 36.19 |

Table 2: Comparison of the closed-loop simulation results for the alleviation of blade loads under the cases of different flow velocity and turbulence intensity with flaps actuated by PD-MFAC and the Gain-scheduled PI controller. The abbreviations are: rms (root-mean-square); rd (reduction); TI ( turbulence-intensity); RBM (root-bending moment); BTD (balde tip deflection).

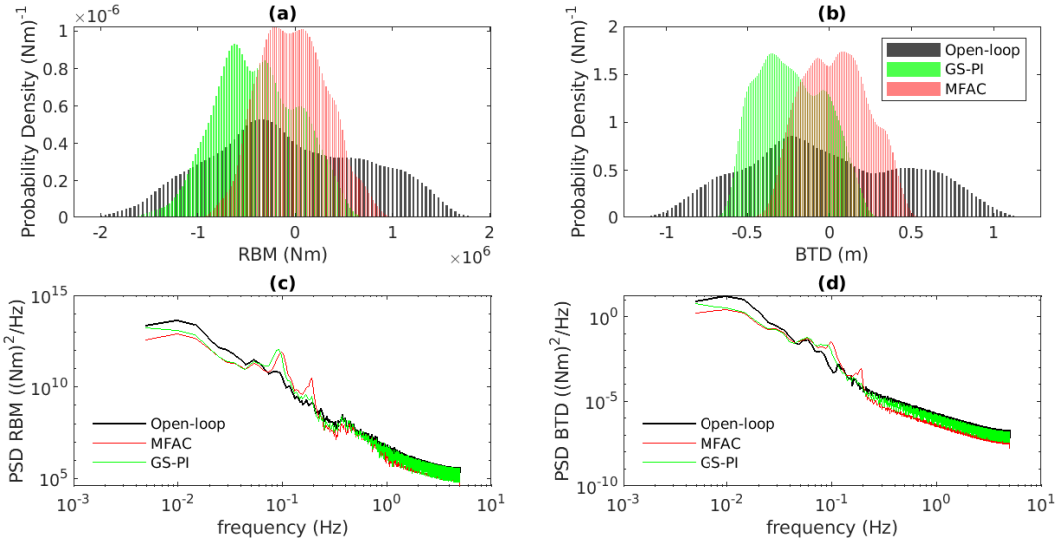


Figure 17: Probability density plot of (a) root bending moment (RBM); (b) blade tip deflection (BTD), and the power spectral density (PSD) of (c) root bending moment (RBM); (d) blade tip deflection (BTD), at a flow velocity of $11m/s$ and turbulence intensity of 6%.

reduction of the full range of frequency load. It is shown in Table 2 that the proposed PD-MFAC has an evident advantage over the traditional model-free adaptive GS-PI controller concerning the reduction of flapwise RBM caused by turbulence. Additionally, as a bonus, the PD-MFAC controller also outperforms the GS-PI controller in the alleviation of BTD caused by turbulence.

## 5. Discussion

An aeroservoelastic model for a wind turbine with TEF configurations has been developed and a model-free PD-MFAC smart rotor controller has been designed for the load alleviation of this wind turbine model. This new model includes an unsteady vortex panel method coupled with a delayed-stall scheme to cope with flow separations. In the regular operating condition, most of the flow around a wind turbine rotors is attached, however, flow separation may frequently happen in the blade root area and for the cases of larger TEF configurations with larger flap deflection angles. Therefore, this new model enables us to more complex operating conditions when the system does not lie in the attached flow regime.

The main purpose of this work is to study the practicability of the PD-MFAC strategy on the

alleviation of the fluctuation load purely caused by the income flow turbulence. The simulation results in the previous section reveal that the PD-MFAC controllers considerably alleviate the flapwise RBM and the BTD caused by turbulence. The excellent performance of the PD-MFAC scheme on the load alleviation of wind turbines through smart rotor control has been thoroughly demonstrated. The results pave the way for more efficient control strategies of larger and more flexible structures, such as wind turbines.

## 6. Conclusions

This work has studied the modeling and load alleviation control method of smart rotor wind turbines driven by a novel PD-MFAC scheme.

1. The newly built aerodynamic model is capable of dealing with separating flows, in this way to give a relatively high fidelity modeling of the wind turbine dynamics controlled by a TEF of any size and rotates at any deflection angles. The TEF deflection affects the aerodynamic force coefficients in several ways: (a) changing the equivalent camber-line, therefore, adjusting the linear force; (b) disturbing the separating bubbles, subsequently, changing the nonlinear force; (c) causing the rolling-up of a trailing edge vortex, as a result, altering the force coefficients through an up-wash effect.
2. As an extension to the previous work, the merit of the novel PD-MFAC strategy has been fully explored here for the effective dynamic load reduction of flapwise RBM on the wind turbines using a TEF control system. The PD-MFAC shows privileges with regard to alleviating the turbulent load in comparison to classical GS-PI control algorithms.
3. A substantial effective turbulent load reduction has been achieved using the PD-MFAC, with an rms RBM reduction of 50.29 - 56.44% and an rms BTD reduction of 54.53 - 62.12%.
4. The PD-MFAC scheme is easy to implement on real systems since it only depends on the real-time input and output data measured from the plant. And the PD-MFAC flap controller has shown its great effectiveness in both tuned case and other cases as shown in Table 2.

In summary, a novel aeroservoelastic model of middle fidelity capable of dealing with flow separations has been developed. This new model has been used to study the dynamics of the reference HAWT under the control of TEFs with a size of 15% chord length and with any deflection angles. This nonlinear aeroservoelastic model consists of a geometrically non-linear composite beam

model for the structural response of the tower/blades assembly and a VPM-based aerodynamic model for the aerodynamic forces acting on the blades. It is coupled with nonlinear aerodynamics including separating flows and could be used to analyze the detailed flow field. A novel PD-MFAC algorithm has been used to actuate the TEF deflections in order to alleviate the turbulent dynamic load on the wind turbine rotors. Through numerical simulations on the open-loop and closed-loop systems, the PD-MFAC shows satisfying turbulent load reduction in various cases. In comparison to the classical GS-PI control algorithms, the PD-MFAC control scheme has better performance in reducing the oscillation of RBM and BTD, especially for the off-design cases. Moreover, the probability density distribution analysis showed that the performance of PD-MFAC is better than the traditional GS-PI controller. And this advantage is even greater in off-design conditions. The power spectral density analysis indicated that for most of the tested cases, the PD-MFAC is superior to the GS-PI in most of the frequency domains except in a frequency between 0.1 Hz and 0.2 Hz. In the future work, (a) the optimal size of the TEF which offers a better control performance could be studied; (b) the wake effect and the three-dimensional effect could be included; (c) the load alleviation of a larger wind turbine (e.g. 20MW), could be studied using the proposed model and control strategy.

## Declaration of competing interest

The authors declare that they have no known competing financial interests or personal relationships that could have appeared to influence the work reported in this paper.

## Acknowledgements

This work has received funding from the European Union's Horizon 2020 research and innovation programme under the Marie Sklodowska-Curie grant agreement No.765579.

## References

[1] F. Porté-Agel, M. Bastankhah, S. Shamsoddin, Wind-turbine and wind-farm flows: A review, Boundary-Layer Meteorology (174) (2020) 1–59.

[2] E. Ferede, F. Gandhi, Load alleviation on wind turbines using camber morphing blade tip., Wind Energy Symposium, 2021.

[3] M. O. L. Hansen, J. N. Sørensen, S. Voutsinas, N. Sørensen, H. A. Madsen, State of the art in wind turbine aerodynamics and aeroelasticity, Progress in aerospace sciences 42 (4) (2006) 285–330.

[4] M. Z. Akhter, F. K. Omar, Review of flow-control devices for wind-turbine performance enhancement, Energies (14) (2021) 1268.

[5] S. M. Barr, J. W. Jaworski, Optimization of tow-steered composite wind turbine blades for static aeroelastic performance, Renewable Energy 139 (2019) 859–872. doi:https://doi.org/10.1016/j.renene.2019.02.125.
URL https://www.sciencedirect.com/science/article/pii/S0960148119302903

[6] W. Yinan, Aeroelastic modelling and control of very flexible air vehicles using a nonlinear modal formulation, Ph.D. thesis (2015).

[7] E. Branlard, The blade element momentum (BEM) method, 2017, pp. 181–211. doi:10.1007/978-3-319-55164-7_10.

[8] S. Xie, An actuator-line model with lagrangian-averaged velocity sampling and piecewise projection for wind turbine simulations, Wind Energy n/a (n/a). arXiv:https://onlinelibrary.wiley.com/doi/pdf/10.1002/we.2619, doi:https://doi.org/10.1002/we.2619.

[9] J. Liang, Y. Qiu, M. Zhao, S. Kang, H. Lu, The modeling and numerical simulations of wind turbine generation system with free vortex method and simulink, Energy Conversion and Management 103 (2015) 762–777. doi:https://doi.org/10.1016/j.enconman.2015.07.006.
URL https://www.sciencedirect.com/science/article/pii/S0196890415006573

[10] X. Cai, Y. Wang, B. Xu, J. Feng, Performance and effect of load mitigation of a trailing-edge flap in a large-scale offshore wind turbine, Journal of Marine Science and Engineering 8 (2). doi:10.3390/jmse8020072.
URL https://www.mdpi.com/2077-1312/8/2/72

[11] B. F. Ng, H. Hesse, R. Palacios, J. M. R. Graham, E. C. Kerrigan, Aeroservoelastic state-space

vortex lattice modeling and load alleviation of wind turbine blades, Wind Energy 18 (7) (2015) 1317–1331.

[12] B. F. Ng, R. Palacios, E. C. Kerrigan, J. M. R. Graham, H. Hesse, Aerodynamic load control in horizontal axis wind turbines with combined aeroelastic tailoring and trailing-edge flaps, Wind Energy 19 (2) (2016) 243–263.

[13] B. F. Ng, R. Palacios, J. M. R. Graham, Model-based aeroelastic analysis and blade load alleviation of offshore wind turbines, International Journal of Control 90 (1) (2017) 15–36.

[14] G. Bangga, T. Lutz, Aerodynamic modeling of wind turbine loads exposed to turbulent inflow and validation with experimental data, Energy 223 (2021) 120076. doi:https://doi.org/10.1016/j.energy.2021.120076.
URL https://www.sciencedirect.com/science/article/pii/S036054422100325X

[15] W. D. K. Cavens, A. Chopra, A. F. Arrieta, Passive load alleviation in wind turbine blades from selectively compliant bi-stable morphing flaps, AIAA Scitech Forum (2019).

[16] T. K. Barlas, G. A. M. van Kuik, Review of state of the art in smart rotor control research for wind turbines, Progress in Aerospace Sciences 46 (1) (2010) 1–27.

[17] C. Plumley, W. Leithead, P. Jamieson, E. Bossanyi, M. Graham, Comparison of individual pitch and smart rotor control strategies for load reduction, in: Journal of Physics: Conference Series, Vol. 524, IOP Publishing, 2014, p. 012054.

[18] D. Ossmann, P. Seiler, C. Milliren, A. Danker, Field testing of multi-variable individual pitch control on a utility-scale wind turbine, Renewable Energy 170 (2021) 1245–1256.

[19] A. Rezaeiha, R. Pereira, M. Kotsonis, Fluctuations of angle of attack and lift coefficient and the resultant fatigue loads for a large horizontal axis wind turbine, Renewable Energy 114B (2017) 904–916. doi:10.1016/j.renene.2017.07.101.

[20] C. David, A. Mazen, D. Domenico Di, S. Guillaume, Data-driven fatigue-oriented mpc applied to wind turbines individual pitch control, Renewable Energy (107) (2021) 1008 – 1019.

[21] R. Unguran, V. Petrovic, L. Y. Pao, M. Kuhn, Smart rotor control of wind turbines under actuator limitations, American Control Conference (2019) 3474–3481.

[22] F. Samara, D. A. Johnson, In-blade measurements of cyclic loading on yawed turbines with trailing edge flap, Journal of Physics: Conference Series (2020) 1452.

[23] L. Bergami, N. K. Poulsen, A smart rotor configuration with linear quadratic control of adaptive trailing edge flaps for active load alleviation, Wind Energy 18 (4) (2015) 625–641.

[24] X. Sun, Q. Dai, M. Menon, F. Ponta, Design and simulation of active external trailing-edge flaps for wind turbine blades on load reduction, Journal of Aerospace Engineering 30 (5) (2017) 04017062. doi:10.1061/(ASCE)AS.1943-5525.0000771.

[25] W. Zhang, X. Bai, Y. Wang, Y. Han, Y. Hu, Optimization of sizing parameters and multi-objective control of trailing edge flaps on a smart rotor, Renewable Energy 129 (2018) 75–91. doi:https://doi.org/10.1016/j.renene.2018.05.091.
URL https://www.sciencedirect.com/science/article/pii/S0960148118306165

[26] W. Zhang, Y. Wang, R. Liu, H. Liu, X. Zhang, Unsteady aerodynamic modeling and control of the wind turbine with trailing edge flap, Journal of Renewable and Sustainable Energy 10 (6) (2018) 063304. arXiv:https://doi.org/10.1063/1.5052023, doi:10.1063/1.5052023.
URL https://doi.org/10.1063/1.5052023

[27] K. He, L. Qi, L. Zheng, Y. Chen, Combined pitch and trailing edge flap control for load mitigation of wind turbines, Energies 11 (10). doi:10.3390/en11102519.
URL https://www.mdpi.com/1996-1073/11/10/2519

[28] R. Feil, N. Abbas, P. Bortolotti, N. Johnson, B. Mertz, Distributed aerodynamic control using active trailing-edge flaps for large wind turbines, Journal of Physics: Conference Series 1618 (2020) 042026. doi:10.1088/1742-6596/1618/4/042026.
URL https://doi.org/10.1088/1742-6596/1618/4/042026

[29] J. Li, Y. Wang, X. Zhao, P. Qi, Model free adaptive control of large and flexible wind turbine rotorswith controllable flaps, Renewable Energy.

[30] J. Jonkman, S. Butterfield, W. Musial, G. Scott, Definition of a 5-mw reference wind turbine for offshore system development, National Renewable Energy Laboratory, Golden, CO, Technical Report No. NREL/TP-500-38060.

[31] I. E. Commission, et al., Iec 61400-1: Wind turbines part 1: Design requirements, International Electrotechnical Commission.

[32] Y. Kawashima, T. Uchida, Effects of terrain-induced turbulence on wind turbine blade fatigue loads, Energy and Power Engineering (9) (2017) 843–857.

[33] J. Katz, A discrete vortex method for the non-steady separated flow over an airfoil, Journal of Fluid Mechanics 102 (1981) 315–328. doi:10.1017/S0022112081002668.

[34] M. Raiola, S. Discetti, A. Ianiro, F. Samara, F. Avallone, D. Ragni, Smart rotors: Dynamic-stall load control by means of an actuated flap, AIAA Journal 56 (4) (2018) 1388–1401. arXiv:https://doi.org/10.2514/1.J056342, doi:10.2514/1.J056342.
URL https://doi.org/10.2514/1.J056342

[35] M. Elgammi, T. Sant, A Modified Beddoes–Leishman Model for Unsteady Aerodynamic Blade Load Computations on Wind Turbine Blades, Journal of Solar Energy Engineering 138 (5), 051009. arXiv:https://asmedigitalcollection.asme.org/solarenergyengineering/article-pdf/138/5/051009/6328739/sol_138_05_051009.pdf, doi:10.1115/1.4034241.
URL https://doi.org/10.1115/1.4034241

[36] M. J. Hoffmann, R. Reuss Ramsay, G. M. Gregorek, Effects of grit roughness and pitch oscillations on the naca 4415 airfoildoi:10.2172/266691.
URL https://www.osti.gov/biblio/266691